

Modal decomposition of velocity signals in a plane, turbulent wake

By B. MARASLI, F. H. CHAMPAGNE AND I. J. WYGNANSKI

Department of Aerospace and Mechanical Engineering, University of Arizona,
Tucson, AZ 85721, USA

(Received 9 October 1986 and in revised form 5 March 1988)

The Orr–Sommerfeld equation admits two solution modes for the two-dimensional plane wake. These are the sinuous mode with antisymmetric streamwise fluctuations and the varicose mode with symmetric streamwise fluctuations. The varicose mode is often ignored because its amplification rates are considerably less than those of the sinuous mode. An experimental investigation of the varicose mode in a two-dimensional turbulent wake was undertaken to determine if this mode of instability agrees as well with linear stability theory, as did the sinuous mode in previous experiments (Wygnanski, Champagne & Marasli 1986). The experiments demonstrated that, although it is possible to generate a nearly pure symmetric disturbance wave, it is very difficult to do as the flow is very sensitive to the slightest asymmetries which might be present in the experiments. These asymmetries are preferentially amplified, resulting in the eventual distortion of an initially prominent symmetric wave. It was therefore necessary to decompose phase-averaged measurements of the streamwise component of the velocity fluctuations into their symmetric and antisymmetric parts, and the results were compared with the appropriate theoretical eigenfunctions from linear stability theory. The lateral distribution of the amplitude and the phase of each mode agree reasonably well with their theoretical counterparts from the Orr–Sommerfeld equation. Slowly diverging linear theory predicts the streamwise variation of the sinuous mode quite well, but fails to do so for the varicose mode. An eddy-viscosity model, coupled with the slowly diverging linear equations, predicts the streamwise variation of both modes reasonably well and describes the transverse distributions of the perturbation amplitudes for both modes, but it fails to predict the distribution of phase for the varicose mode.

1. Introduction

Large-scale coherent structures in the small-deficit wake behind a flat plate were observed by Wygnanski, Champagne & Marasli (1986) using combined hot-wire and flow-visualization techniques.† Evidence was presented that these large-scale structures, which resemble the Kármán vortex street in appearance, can be described

† Note the following corrections to Wygnanski *et al.* (1986):

- (i) In table 1, the value of θ for the 6.35 mm diameter cylinder at a Reynolds number of 5800 is 3.51 mm, not 2.64 mm.
- (ii) Equation (2.3) should read:

$$V(t) = \frac{P_1(E_1) - P_2(E_2)}{(A_{3,2} - A_{3,1})}, \quad U(t) = P_1(E_1) + A_{3,1} V.$$

by linear stability theory. Theoretical calculations based on linear, inviscid stability theory showed excellent agreement with the measured transverse distributions of amplitudes and phases of externally imposed sinuous waves on the fully turbulent wake behind the flat plate. When the divergence of the mean flow was incorporated into the analysis, the spatial amplification of the sinuous waves in the streamwise direction was successfully predicted. Although the sinuous disturbances represent the predominant mode of instability from linear theory, the possible importance of the varicose disturbances (those that have a symmetrical streamwise component about the wake centreline) was considered. Varicose disturbances have relatively smaller amplification rates and are usually neglected in stability analyses. The varicose mode, however, may at times dominate the shape of the large structures (Papailiou & Lykoudis 1974; Rockwell, Ongoren & Unal 1985; Williamson 1985) and, even when the prevailing instability is mainly sinuous in nature, a small varicose component was shown to alter the gross behaviour of the calculated streakline patterns (Wygnanski *et al.* 1985). The latter provided the initial motivation for the present study, the purpose of which is to investigate the significance of the varicose mode in two-dimensional, small-deficit, turbulent wakes. One should note that the varicose mode has not been investigated experimentally in either laminar or turbulent wakes, and its existence was by no means assured, particularly in a fully turbulent environment.

2. Description of experiments

The wakes were generated in the University of Arizona's low-speed wind-tunnel facility. The zero-pressure-gradient test section is nominally 61 by 91 cm in cross-section and 6 m long. The speed in the test section was 7.5 m/s for the present experiments, while the free-stream disturbance level in the streamwise velocity component was 0.03%. The tunnel is equipped with chilled water coils to maintain the temperature of the flow constant. The flat-plate wake generator was a solid aluminium plate 30 cm long, 61 cm wide, and 0.635 cm at its point of maximum thickness. The leading edge was rounded, and the trailing edge was tapered to 1 mm thickness over the last 10 cm of the plate surface. Trip wires, placed 3 cm from the leading edge, generated a turbulent boundary layer before the tapered section was reached. The Reynolds number based on the momentum thickness, θ , was approximately 1400 for the present data.

In the previous experiments by Wygnanski *et al.* (1986), sinuous waves were generated by oscillating a small flap (5 mm in length) hinged to the trailing edge of the plate. For the present experiments, sinusoidal varicose disturbances, which are symmetrically distributed about the wake centreline, were generated by oscillating two small flaps 180° out of phase. The flaps were placed symmetrically above and below the plate, approximately 18 cm from the leading edge and just upstream of the tapered trailing-edge region of the plate, as indicated by the sketch shown in figure 1. The insert shown in figure 1 presents details of the flap arrangement. The dashed lines show the maximum range of motion of the flaps, which was set such that the flaps did not touch the plate. Scotch tape was used as the hinge to attach the flaps to the ramps. Nylon ribbons were used to connect the downstream edge of each side of the flaps to matched loudspeakers, which were located on each side of the plate just outside the tunnel sidewalls. The forcing level is specified by the maximum value of the measured r.m.s. of the streamwise component of the perturbation wave at $x/\theta = 200$. For the varicose mode, the maximum occurs at the centreline.

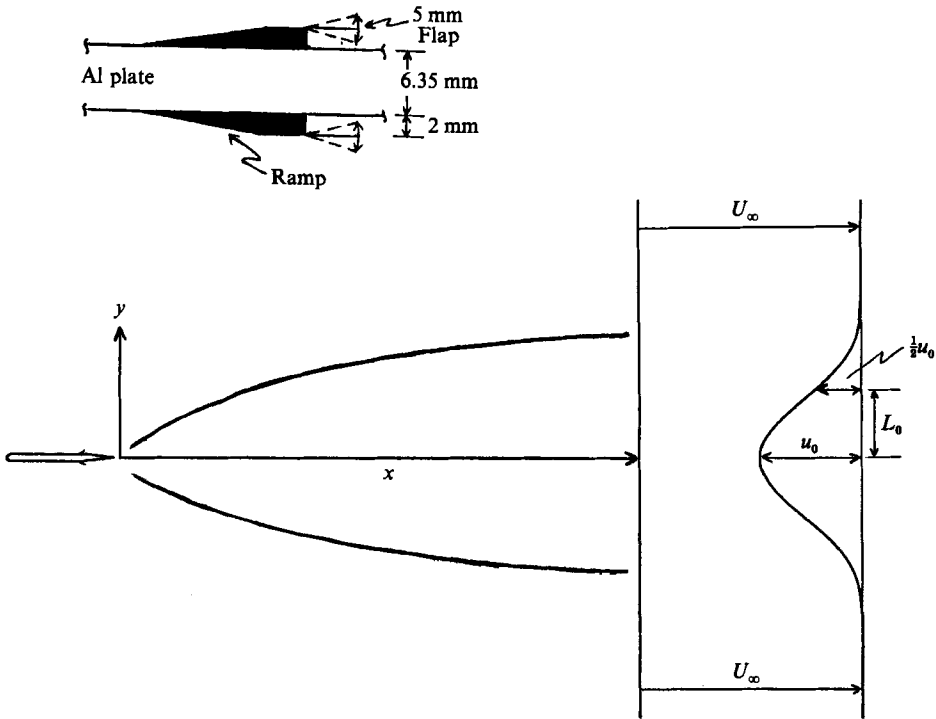


FIGURE 1. Schematic of plate and wake defining the nomenclature. The insert shows the details of the flap arrangement.

3. Theoretical background

The instantaneous streamwise (u) component velocity signal is represented by

$$U = \bar{U} + \tilde{u} + u', \quad (1)$$

where \bar{U} is the mean or time-averaged part, \tilde{u} is the periodic wave contribution, and u' is the turbulent part (Reynolds & Hussain 1972). Another quantity that will be referred to often is the total fluctuating signal,

$$u = \tilde{u} + u'. \quad (2)$$

Assume that the perturbation stream function for a wavy disturbance superimposed on a parallel flow $\bar{U}(y)$ has the form

$$\psi(X, \eta, t) = \text{Re}[\phi(\eta) e^{i(\alpha X - \beta t)}], \quad (3)$$

where $X = x/L_0$, $\eta = y/L_0$, $\beta = 2\pi f L_0/U_\infty$ is the non-dimensional frequency and $\alpha = \alpha_r + i\alpha_i$ is a non-dimensional complex quantity whose real part represents the wavenumber while its imaginary part represents the spatial amplification rate; α is non-dimensionalized by L_0 . The growth or decay of such disturbances, as long as they remain sufficiently small to permit linearization of the equations of motion, are governed by the Orr-Sommerfeld equation which, in non-dimensional form, is given by

$$\left(U^* - \frac{\beta}{\alpha}\right)(\phi'' - \alpha^2\phi) - U^{*''}\phi - \frac{1}{i\alpha Re}(\phi^{iv} - 2\alpha^2\phi'' + \alpha^4\phi) = 0, \quad (4)$$

where $U^* = \bar{U}/U_\infty$; Re is the Reynolds number of the basic flow, chosen here to be $U_\infty L_0/\nu$; U_∞ is the free-stream velocity; L_0 is the wake half-width (see figure 1); and ν is the kinematic viscosity.

At large values of the transverse coordinate, i.e. $\eta \rightarrow \pm \infty$, $U^* \rightarrow 1$, and $U^{*'} \rightarrow 0$, equation (4) reduces to

$$\phi^{iv} - [\gamma^2(\eta) + \alpha^2] \phi'' + \alpha^2 \gamma^2(\eta) \phi = 0, \quad (5)$$

where $\gamma^2(\eta) = i\alpha Re(U^* - \beta/\alpha) + \alpha^2$. This equation has four independent solutions for each side of the flow, which can be described by

$$\phi(\eta) = \sum_{n=1}^4 A_n e^{\eta p_n} \quad \text{as } \eta \rightarrow -\infty, \quad \phi(\eta) = \sum_{n=1}^4 B_n e^{\eta q_n} \quad \text{as } \eta \rightarrow +\infty, \quad (6)$$

where

$$p_{1,2} = \pm \alpha, \quad p_{3,4} = \pm \gamma(-\infty), \\ q_{1,2} = \pm \alpha, \quad q_{3,4} = \pm \gamma(+\infty).$$

The disturbances must decay exponentially with increasing distance from the centreline of the wake, and this decay leads to $A_2 = A_4 = B_1 = B_3 = 0$.

In order to satisfy these boundary conditions, a shooting technique described by Betchov & Szewczyk (1963) is used for low Reynolds numbers ($U_\infty L_0/\nu < 800$). For large Reynolds numbers, a Gram-Schmidt orthonormalization technique is used, as described by Bellman & Kalaba (1985) and utilized by Wazzan, Okamura & Smith (1968) and others.

The inviscid case is much simpler and the boundary conditions are

$$\phi' \pm i\alpha\phi = 0, \quad (7)$$

for $\eta \rightarrow \pm \infty$, which requires the disturbance to decay exponentially on both sides of the wake.

4. Generation of varicose mode

It was extremely difficult to generate purely symmetrical disturbances because any lack of symmetry in the generating mechanism resulted in a combination of modes. The results of one attempt to generate a pure varicose mode are given in figure 2. Data on the transverse distributions of \bar{u}^2/u_0^2 for downstream locations in the range $100 < x/\theta < 1400$ are shown. The flaps were driven 180° out of phase at 35 Hz, and a rake of nine hot wires was used to obtain the data. This excitation frequency corresponds to a Strouhal number based on momentum thickness, $St = f\theta/U_\infty$, of 0.0127. The maximum value of the r.m.s. of the u -component of the perturbation velocity at $x/\theta = 200$ was $(\tilde{u}_{\text{rms}}/u_0)_{\text{max}} = 11.7\%$. The data indicate that the flow is self-preserving, but the self-preserving distribution for this case differs slightly from that for the unforced case (\bar{u}^2/u_0^2), which is shown in figure 3 for comparison. The flow in both cases is fully turbulent and, in the forced case, only $\sim 10\%$ of the total fluctuations are coherent, which is also reflected by comparing the maximum value of $\overline{(\tilde{u} + u')^2}/u_0^2$ for the forced case and \bar{u}'^2/u_0^2 for the unforced case. The ratio of $\bar{u}_{\text{CL}}^2/\bar{u}_{\text{max}}^2$ is 0.76 for the unforced case and 0.80 for the forced case. One should note that, in general, due to the presence of the artificially introduced coherent motion, the flow is not expected to be as self-preserving as the unforced case. The fact that it is should be attributed to the low level of forcing, which perhaps justifies the application of linear theory.

The mean velocity distributions for each wake are self-preserving, although the

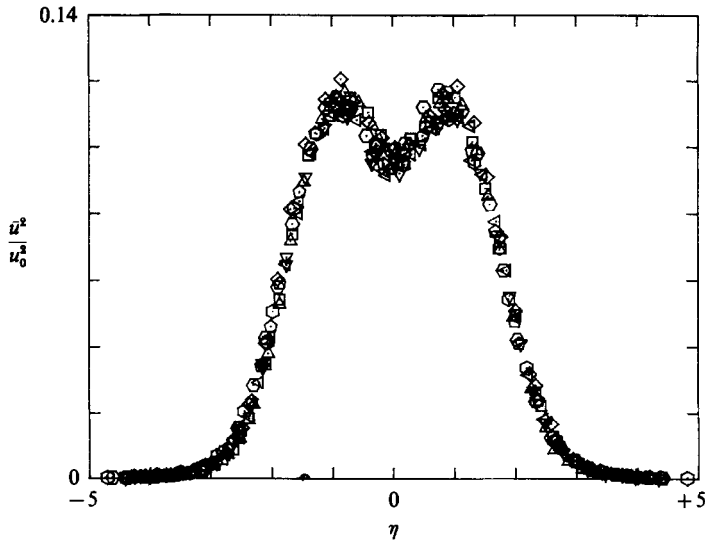


FIGURE 2. The measured distribution of \bar{u}^2/u_0^2 for the varicose forced wake. Different symbols represent different downstream locations in the range $100 < x/\theta < 1400$.

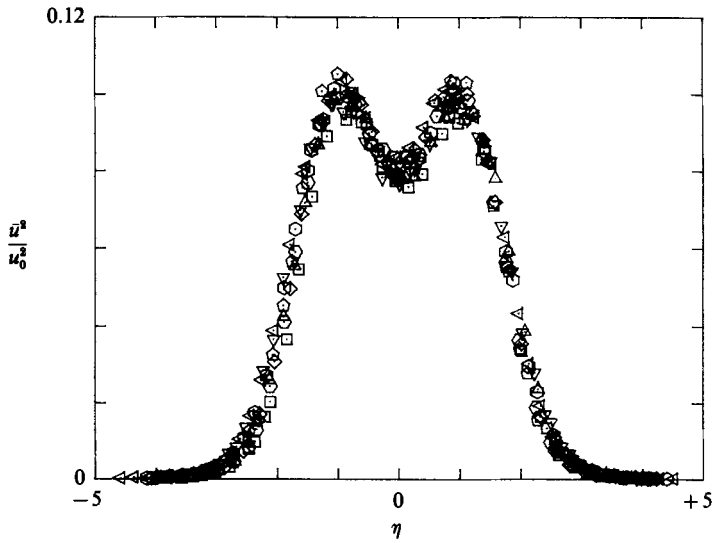


FIGURE 3. The measured distribution of \bar{u}^2/u_0^2 for the unforced wake.

wakes developed at slightly different rates in the downstream direction. The streamwise development of the characteristic scales u_0 and L_0 can be expressed as

$$\left[\frac{U_\infty}{u_0} \right]^2 = \frac{x-x_0}{\theta W_0^2}, \tag{8}$$

$$\left[\frac{L_0}{\theta} \right]^2 = \Delta_0^2 \frac{x-x_0}{\theta}, \tag{9}$$

where W_0 and Δ_0 are constants for a given self-preserving wake. The values of W_0 and Δ_0 for the unforced wake are 1.68 and 0.304, respectively; while those for the varicose

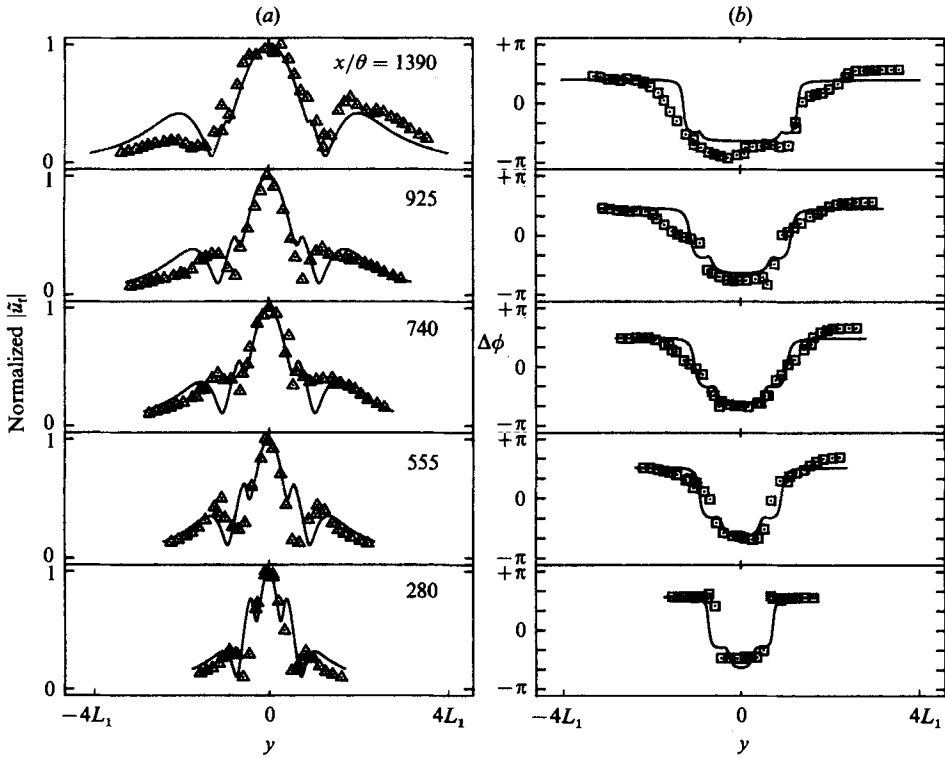


FIGURE 4. (a) The amplitude distributions of the u -component of the disturbance wave for $f = 35$ Hz: \triangle , phase-averaged measurements; —, theoretical varicose L_1 is the value of L_0 at $x/\theta = 1390$. (b) The phase distributions of the disturbance wave: \square , phase-averaged measurements; —, theoretical varicose.

forced wake are 1.62 and 0.312. The mean field is therefore affected slightly by the forcing. The virtual origin $x_0 = 0$ and the momentum thickness $\theta = 2.9$ mm for all sets of data presented in this paper. The self-preserving mean velocity profiles are, however, effectively identical for the two wakes. That is, plots of the self-preserving function $f(\eta)$, defined by

$$f(\eta) = \frac{U_\infty - \bar{U}(x, y)}{u_0(x)} = \exp[-0.637\eta^2 - 0.056\eta^4], \quad (10)$$

are representative of the profiles for the two wakes.

The distributions of the amplitudes and phases of the velocity perturbations associated with the varicose waves are shown in figure 4(a, b) for five downstream locations. The data, shown by the symbols, were obtained by recording the velocity signal together with the sinusoidal signal activating the flaps. The velocity signals were phase-averaged over 500 cycles of the flap motion, and the Fourier transform applied on the phase-averaged data provided the amplitudes and phase estimates of the spectral elements of the coherent velocity field. The subscript f denotes the component at the fundamental forcing frequency. The abscissa in the figures is dimensional y and the scaling is identical in all figures. The ordinate in figure 4(a) is normalized amplitude and in figure 4(b) is relative phase shift. The results are displayed in this form to indicate the downstream evolution of the wave. The solid lines represent the theoretical results computed from inviscid, linear stability theory

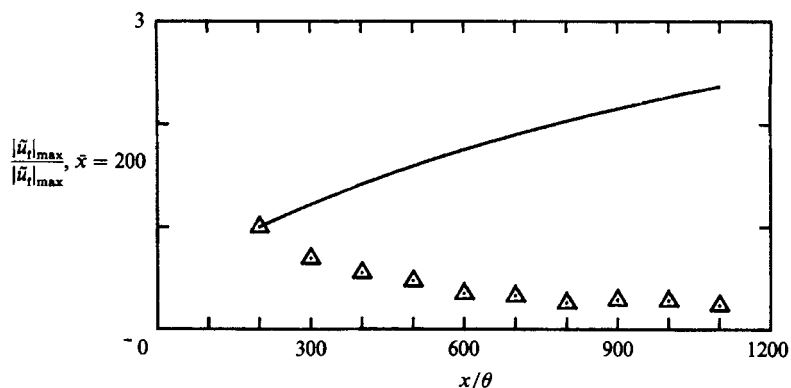


FIGURE 5. The downstream growth of the centreline value of the u -component disturbance amplitude, $f = 35$ Hz: Δ , measurements; —, theoretical linear theory including effects of mean flow divergence.

using the local measured mean velocity profiles. The measured and theoretical amplitude results are normalized by their respective maxima for each downstream location. The disturbance wave remained symmetric for more than 1000 momentum thicknesses before becoming contaminated by asymmetries. There is reasonable agreement between the experimental and theoretical results, even though the wake is fully turbulent. Some of the fine details, such as the minor lobes closest to the centreline shown in the theoretical curves, are not evident in the experimental results. These lobes will subsequently be shown to be related in part to the use of the inviscid approximation.

Another set of measurements was taken at a higher excitation frequency of 50 Hz, $St = 0.0179$, which according to linear theory should evolve sooner. The forcing level at the initial measuring station $x/\theta = 200$ was $(\tilde{u}_{rms}/u_0)_{max} = 11.5\%$. Again, the agreement between the experimental and theoretical amplitude and phase distributions was satisfactory. In this case, the disturbance wave was not detectable beyond $x/\theta > 700$.

The success of inviscid linear theory ends for the varicose mode when the streamwise growth of the disturbance is considered. A comparison between the experimental and theoretical results for the 35 Hz case is shown in figure 5. The theoretical prediction includes the effects of the divergence of the mean flow using the analysis presented by Wygnanski *et al.* (1986). The theoretical results indicate a monotonic growth of the amplitude of \tilde{u}_t on the centreline of the wake, whereas the measurements show a decrease. This discrepancy will be discussed in a subsequent section.

The experiments demonstrated that it is possible to generate a nearly pure symmetric disturbance wave. The difficulty encountered in doing so indicates that the flow is very sensitive to the slightest asymmetries which might be present in the experiments. These asymmetries are preferentially amplified, resulting in the eventual destruction of an initially prominent symmetric wave. It was therefore evident that the total phase-averaged velocity signal should be decomposed into its symmetric and antisymmetric modes in order to study the downstream evolution and interaction.

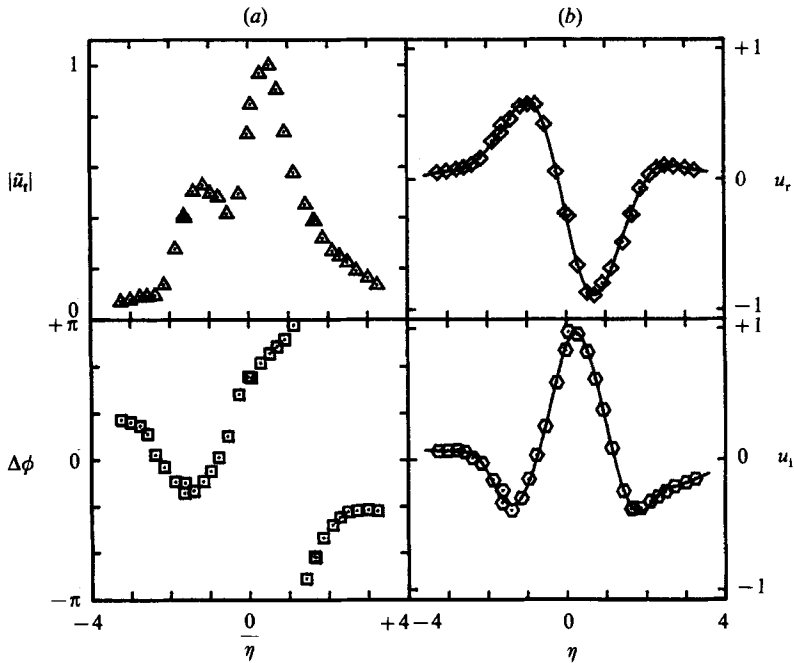


FIGURE 6. (a) The transverse distribution of the amplitude and phase of the forced wave in polar form. (b) As (a) but presented in terms of real and imaginary parts. Symbols represent data, while the solid lines represent the curve fit to data.

5. Decomposition procedure

To decompose the phase-averaged data into modes, we shall take advantage of the fact that the sinuous and varicose modes have \tilde{u} -components that are odd and even functions, respectively, of y . Therefore, if we separate the measured perturbations into odd and even parts, we may have a means of separating the sinuous and varicose modes. The amplitude and phase distributions of the separated parts would then have to be examined and compared to the theoretical distributions of the sinuous and varicose modes.

The decomposition procedure is given as follows. First, we measured the transverse distribution of the phase-averaged u -component, \tilde{u} , using an array of nine hot wires. Typically, 36 points were used to define a distribution. The phase-averaged data for each y -position was Fourier transformed to determine \tilde{u}_\perp , the component of the velocity perturbation associated with the forced wave at the forcing frequency. The transverse distribution of the amplitude and phase (polar form) of \tilde{u}_\perp are shown in figure 6(a) for some example data. The triangles and squares represent the data. The same data are shown in figure 6(b) but in terms of their real and imaginary parts, where the subscripts r and i represent real and imaginary, respectively. To obtain the odd and even parts of these distributions, the centreline location was estimated using the measured mean velocity profile. Then, as we generally did not have data at exactly equidistant positions about the centreline, we fitted a curve to the measured data. Fourier series in y (or η) were used as a curve fit to the real and imaginary parts separately. The fitted curves are shown for the example data by the solid lines in figure 6(b). The curve fit to each was separated into its odd and even parts, indicated in figure 7(a, b) by the dashed lines and solid lines, respectively. The

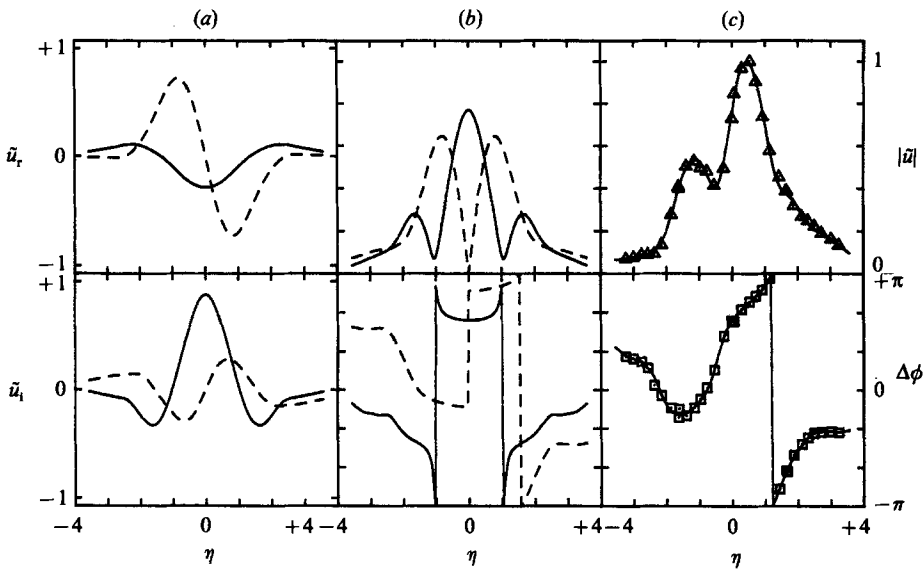


FIGURE 7. (a) The odd and even parts of the curve fit: ---, odd part, —, even part. (b) As in (a) but expressed in polar form. (c) —, superposition of odd and even parts; symbols represent original data.

respective odd and even parts are expressed in polar form in figure 7(b), while their superposition, which restores the original data, is shown in figure 7(c) by the solid lines. The symbols in figure 7(c) represent the original data, which agree well with the estimated distributions obtained from the curve fits to the real and imaginary parts. This agreement demonstrates that the curve fitting was done satisfactorily without introducing any bias. Note, for the example data, that the amplitude distribution has a large even component, although it is asymmetric. One should also recognize the resemblance of the decomposed parts, shown in figure 7(b), to the sinuous and varicose modes computed from linear stability theory.

6. Combined modal forcing of the wake

By applying a small phase difference to the relative motion of the two flaps, a sinuous component was also introduced. This provides a means of simultaneously forcing the wake with both modes to study their possible interaction. The results of combined forcing at a frequency of 28 Hz ($St = 0.0109$) in terms of the lateral distribution of \bar{u}^2/u_0^2 are shown in figure 8. The forcing level $(\tilde{u}_{rms}/u_0)_{max}$ was 12.0% at $x/\theta = 200$. The flow appears to be self-preserving, but the \bar{u}^2 distribution is asymmetric. The mean velocity profile retains its symmetry, and the mean spreading rate is given by the values of W_0 and Δ_0 equal to 1.61 and 0.312, respectively. Again, the amplitude of the coherent fluctuations is small, and the wake maintains a nearly self-preserving form.

The measured amplitude and phase distributions of \tilde{u}_r for five downstream locations are shown in figure 9. The ordinate for each is the normalized amplitude of \tilde{u}_r . The abscissa is y and has the same scale for each plot. The wake growth with x is evident. The amount of asymmetry changes initially with x but appears to remain nearly constant in the far wake ($x/\theta > 750$). The solid lines in figure 9 will be discussed at the end of §7. These distributions were decomposed into their odd and

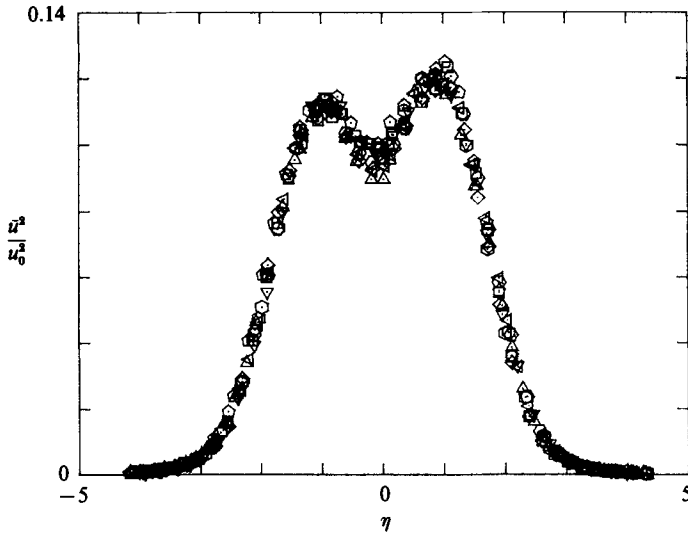


FIGURE 8. The measured distributions of \bar{u}^2/u_0^2 for the forced wave. Combined mode forcing, $f = 28$ Hz.

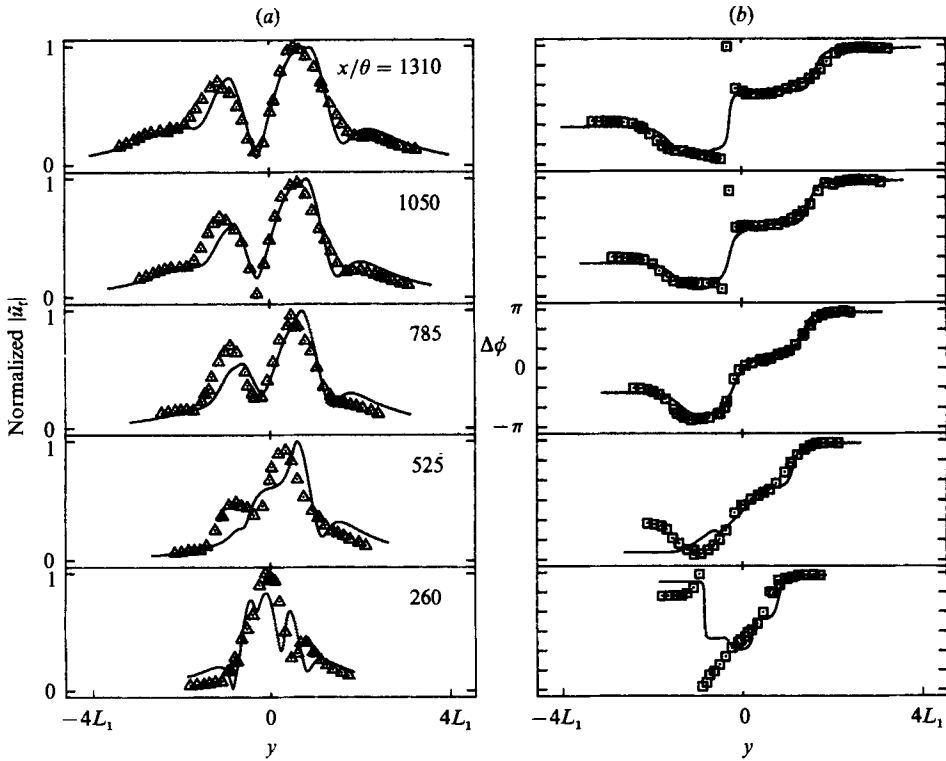


FIGURE 9. (a) The amplitude distributions of the u -component of the disturbance wave: Δ , the measured phase-averaged results; —, linear superposition of modes using equation (11). L_1 is the value of L_0 at $x/\theta = 1310$. (b) The phase distributions of the u -component of the disturbance wave: \square , measured; —, superposition of theoretical modes.

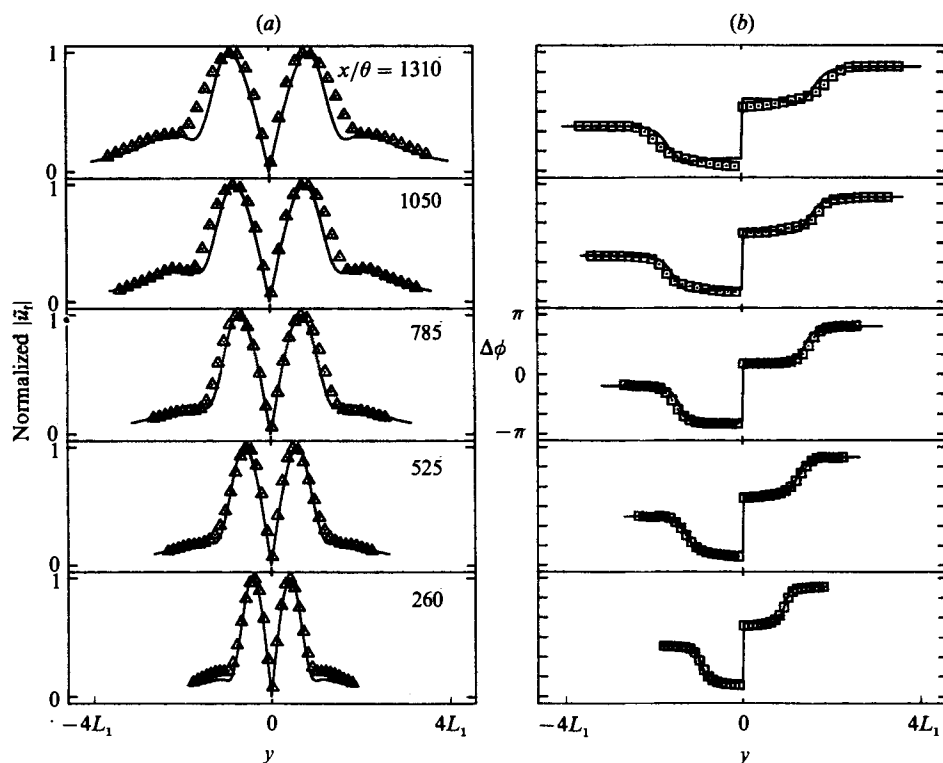


FIGURE 10. (a) The amplitude distributions of the antisymmetric component: Δ , measured; —, theoretical sinusoid. L_1 is the value of L_0 at $x/\theta = 1310$. (b) The phase distributions of the antisymmetric component: \square , measured; —, theoretical sinusoid.

even parts. The resulting odd part for each downstream location is plotted in figure 10(a), designated by triangles. The ordinate is the normalized amplitude and the abscissa is y , again. The solid lines represent the normalized amplitude of the theoretical sinusoid mode computed from linear, inviscid stability theory using the measured mean velocity profiles. The comparison between the theoretical and measured phase distributions is shown in figure 10(b). The agreement between the measured odd parts and the theoretical sinusoid mode is excellent. Thus, the measured odd part undoubtedly corresponds to the sinusoid mode obtained from the stability theory.

The amplitude and phase distributions for the even parts at each downstream location are shown in figure 11(a, b). The solid lines represent the theoretical varicose distributions. The agreement is quite satisfactory, though it is not as good as for the sinusoid model, but the even part appears to correspond to the varicose mode of linear stability theory.

The relative intensity of the two modes was obtained by integrating the amplitude distributions across the flow for each mode and taking the ratio of the two. The downstream evolution of the ratio is shown in figure 12. Initially, the amplitude of the varicose mode is about twice that of the sinusoid mode but, in accordance with linear theory (parallel flow), the sinusoid mode eventually dominates and an equilibrium ratio of $A_v/A_s = 0.5$ is reached for $x/\theta > 800$, at least for this particular experiment. It is surprising that a non-vanishing constant ratio is achieved, but the generality of this intriguing result is yet to be established.

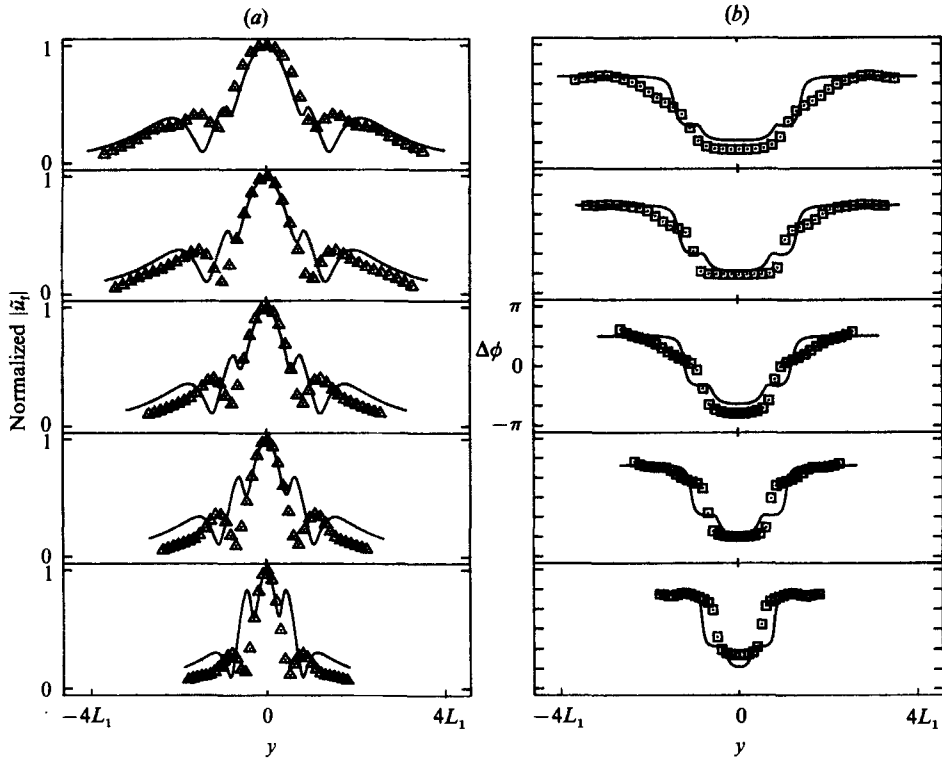


FIGURE 11. (a) The amplitude distributions of the symmetric component: Δ , measured; —, theoretical varicose. L_1 is the value of L_0 at $x/\theta = 1310$. (b) The phase distributions of the symmetric component: \square , measured; —, theoretical varicose.

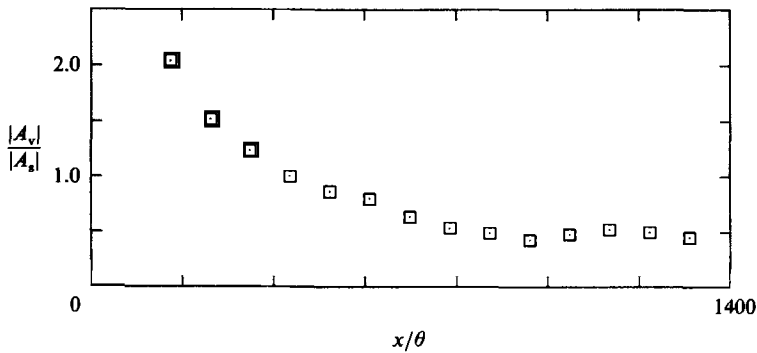


FIGURE 12. The relative ratio of the two modes.

The spatial growth of the maximum of the sinuous and varicose components of the disturbance wave is shown in figure 13. The slowly diverging analysis presented in Wagnanski *et al.* (1986) was used to obtain the theoretical prediction for each mode represented by the solid lines. The growth of the sinuous mode is predicted quite well by linear theory, as it was in the case presented by Wagnanski *et al.* (1986). The growth of the varicose mode is not well predicted, however, which was also the case for the purely varicose forcing presented previously. An interesting point to note regarding the spatial amplification of the two modes is that, for the same mean flow

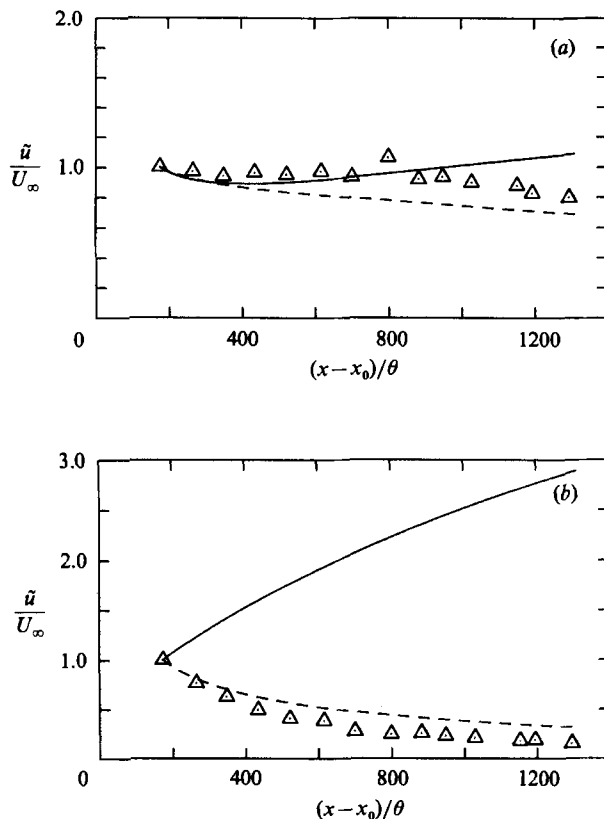


FIGURE 13. The spatial variation of the maximum value of \tilde{u}_t for $f = 28$ Hz for (a) the sinuous mode and (b) the varicose mode: \triangle , measured; —, inviscid; ---, $Re_\theta = 30$.

and frequency, the varicose mode is predicted to amplify more than the sinuous mode, although the growth rates from parallel theory are much larger for the latter. This point is confirmed by T. F. Balsa (private communication), who performed the calculations independently, utilizing a different computational scheme. Apparently, the divergence effects which inhibit the rate of amplification of a particular mode are much more severe on the propagation of the sinuous mode than the varicose mode. The experimental results, however, do not seem to support this theoretical observation and some conjectures will be presented regarding this discrepancy and its possible implications for the evolution of laminar near wakes. The dashed lines will be discussed subsequently.

7. Superposition of modes

The agreement between the amplitudes and phases of the odd and even parts of the phase-averaged data and the theoretical sinuous and varicose modes (figures 10 and 11) suggests that a proper superposition of the theoretical modes should agree well with the experimental phase-averaged results.

The proposed superposition is as follows:

$$\phi'_{TOT}(y) = c_s \phi'_s(y) + c_v \phi'_v(y), \tag{11}$$

where ϕ'_{TOT} = measured disturbance (\tilde{u}_t), ϕ'_s = theoretical sinuous eigenfunction, ϕ'_v = theoretical varicose eigenfunction; and c_s and c_v are complex constants given by

$$c_s = \frac{\int_{-\infty}^{\infty} \phi'_{\text{TOT}} \phi'_s dy}{\int_{-\infty}^{\infty} \phi'_s \phi'_s dy}, \quad (12)$$

and

$$c_v = \frac{\int_{-\infty}^{\infty} \phi'_{\text{TOT}} \phi'_v dy}{\int_{-\infty}^{\infty} \phi'_v \phi'_v dy}. \quad (13)$$

The composite theoretical curves, indicated by the solid lines, are compared with the experimental data in figure 9 and, as expected, the agreement between the two is quite good.

8. Effects of viscosity

The Reynolds number based on the free-stream velocity, the half-width of the wake, and the molecular viscosity is about 10^4 for most of the data presented here and, therefore, viscous effects are not expected to be of importance. However, if one considers the appropriate velocity scale to be the velocity deficit of the wake, which is typically 5% of the free-stream velocity, the ensuing Reynolds numbers are of the order of 500. This motivated a brief study of the stability of the viscous wake. For this purpose, the full Orr–Sommerfeld equation (4) has to be considered together with the appropriate boundary conditions (presented in §3). The Orr–Sommerfeld equation was solved numerically using the Gram–Schmidt orthonormalization technique with double precision complex arithmetic, which provided valid solutions for rather high Reynolds numbers.

The calculations were done using the mean-flow parameters corresponding to the combined modal forcing experiment. Figure 14(a) shows the amplification rates versus the non-dimensional frequency β of the sinuous mode for a constant value of the velocity deficit $u_0/U_\infty = 12.3\%$, which corresponds to the initial streamwise location of the experiment. Three cases are presented. The solid curve represents the inviscid solution. The dashed line corresponds to the viscous solution for $Re_\theta = U_\infty \theta/\nu = 1400$, and at this Reynolds number the difference between the inviscid and viscous amplification rates is hardly visible. The Reynolds number based on θ is the appropriate choice for the experiments, as θ is the proper lengthscale characterizing the wake generator. Recall that θ is a constant for the zero-pressure-gradient wake. For this velocity deficit, the experimental excitation frequency 28 Hz corresponds to $\beta = 0.282$, and it is amplified. The third curve, which is indicated by the dotted-dashed lines, represents calculations done at a much lower Reynolds number, namely at $Re_\theta = 30$, and the growth rates are more visibly lower than their inviscid counterparts. The reason for the choice of this quite low Re will be evident in the next section. Figure 14(b) shows the calculated growth rates using the parameters corresponding to the final x -station of our measurements ($u_0/U_\infty = 4.5\%$). The nomenclature is the same as in figure 14(a). At this location, $f = 28$ Hz corresponds to $\beta = 0.772$, which is comfortably in the amplified region of all the cases presented. The streamwise variation of the growth rate, $-\alpha_1$, for the sinuous mode is presented

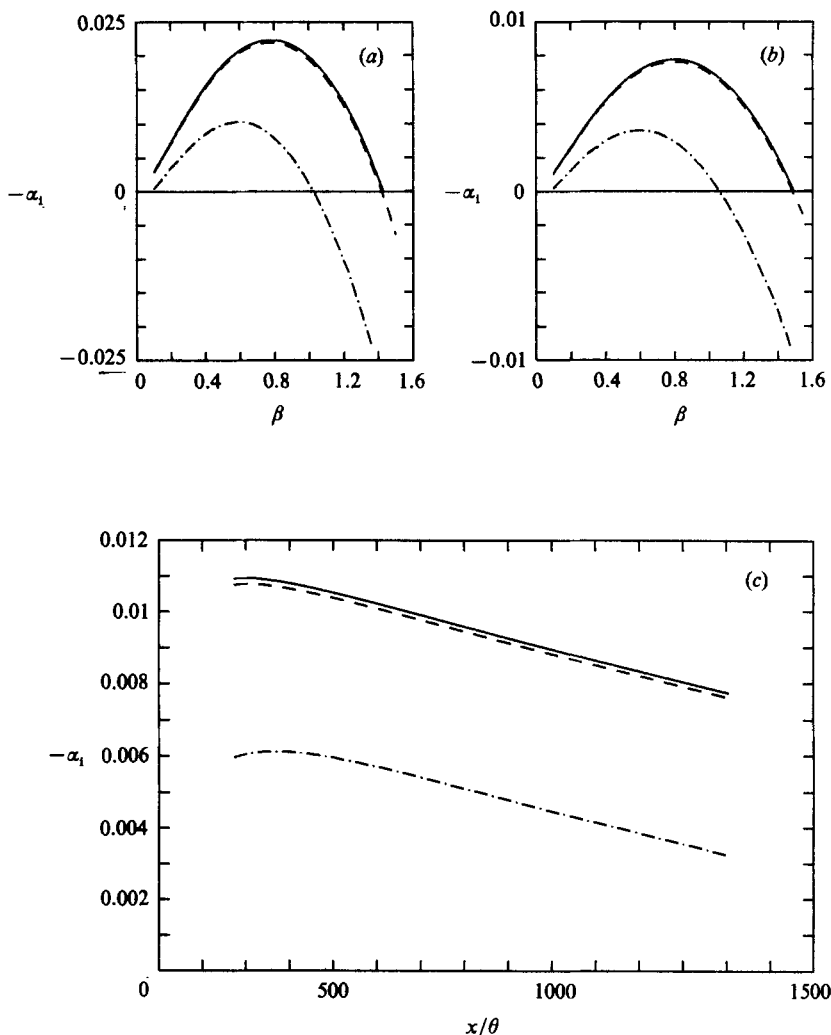


FIGURE 14. Amplification rates for the sinuous mode: (a) versus β , $u_0/U_\infty = 0.123$; (b) versus β , $u_0/U_\infty = 0.045$; (c) versus x/θ ; —, inviscid; ---, $Re_\theta = 1400$; - · -, $Re_\theta = 30$. Recall that α_r is non-dimensionalized by L_0 .

in figure 14(c). For the present case, the amplification rates decay almost linearly with x . It is certainly evident that the viscous effects are negligible for this case. The wavenumber α_r and the phase speed are not shown as they are not significantly affected by viscosity.

The varicose mode is observed to be affected more by viscosity. Figure 15(a, b, c) depicts similar calculations for the varicose mode using the experimental mean-flow parameters. The nomenclature is the same as in figure 14(a, b, c). The growth rates at $Re_\theta = 1400$ are approximately 10% less than their inviscid counterparts. However, this difference cannot explain the discrepancy between the experimental results and the inviscid predictions shown in figure 13(b). But, a dramatic difference is seen for the $Re_\theta = 30$ calculations – the disturbances are damped at this low Reynolds number. Again, the phase speed and α_r are essentially unaffected.

There is no significant change in the shape of the eigenfunction for the sinuous

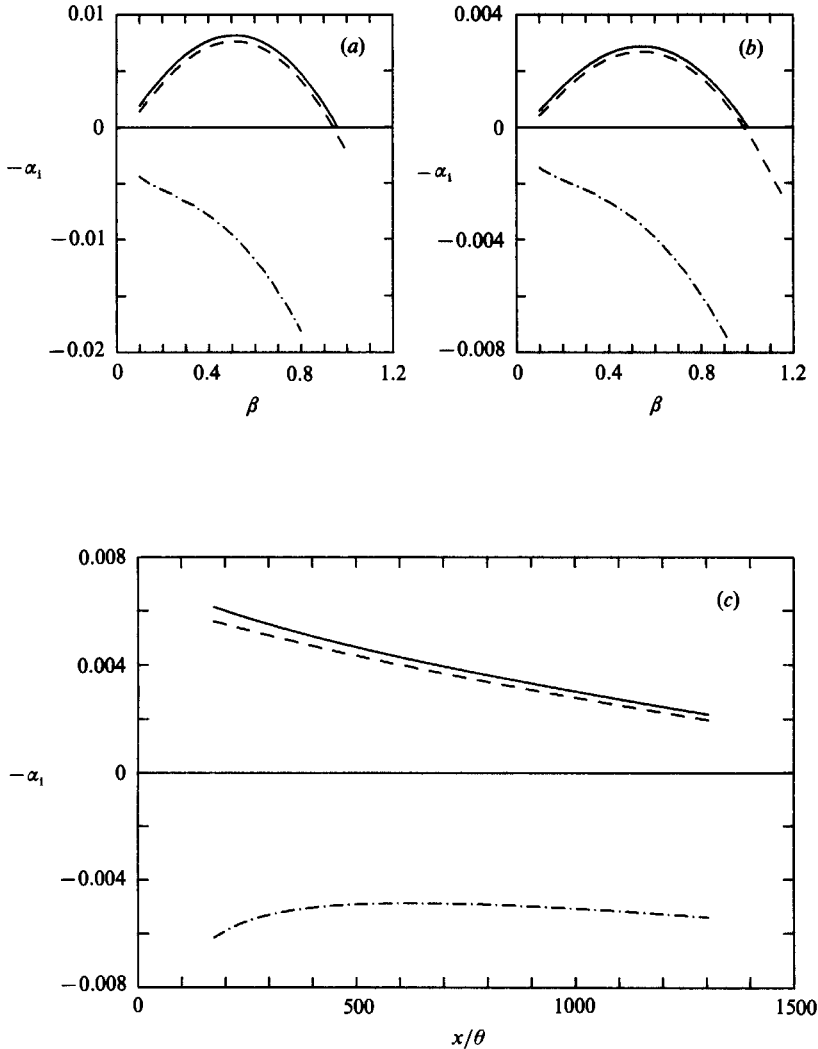


FIGURE 15. Amplification rates for the varicose mode: (a) versus β , $u_0/U_\infty = 0.123$; (b) versus β , $u_0/U_\infty = 0.045$; (c) versus x/θ ; —, inviscid; ---, $Re_\theta = 1400$; - · -, $Re_\theta = 30$.

mode when viscous effects are included, as can be seen from figure 16(a). The u -amplitude distribution of the velocity perturbation for the inviscid case is compared with the viscous solutions for $Re_\theta = 1400$ and 30. The distributions are normalized using their respective maxima. The parameters corresponding to $x/\theta = 400$ of our measurements were used in the computations of the presented cases ($u_0/U_\infty = 8.1\%$, $\beta = 0.428$). The shape of the predicted varicose eigenfunction is more significantly affected, as viscosity tends to eliminate the kinks occurring in the u -amplitude distribution, as shown in figure 16(b). The velocity gradients in the varicose mode are much larger than those occurring in the sinuous mode, thus making the higher-derivative terms in (4) of considerable importance, and the viscosity works towards smoothing those large gradients.

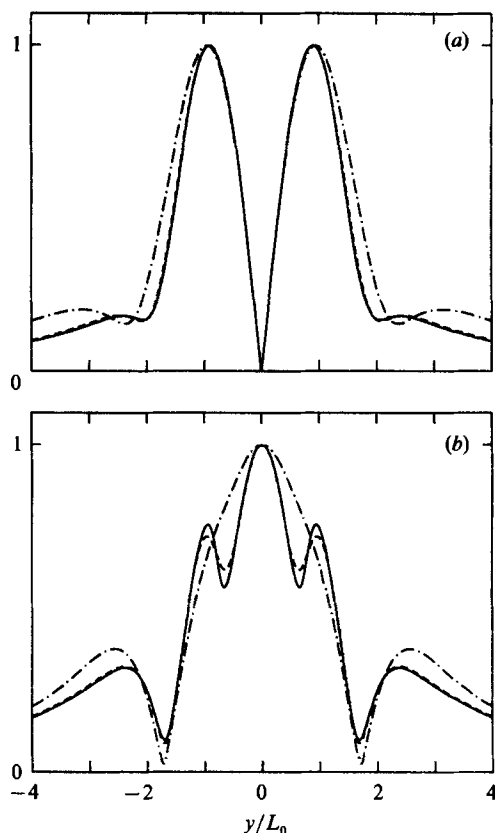


FIGURE 16. The u -amplitude distributions for (a) the sinuous mode and (b) the varicose mode where $u_0/U_\infty = 0.081$ and $\beta = 0.428$: —, inviscid; ---, $Re_\theta = 1400$; -·-, $Re_\theta = 30$.

9. Effects of turbulence

The effects of the turbulent fluctuations on the spatial propagation of the perturbation waves are completely ignored in the present model. As already mentioned, all theoretical results are computed from linear stability theory using the measured local mean velocity profiles. The base flow is fully turbulent rather than laminar. The viscous effects, as discussed in the previous section, are estimated using the same mean velocity profiles along with the molecular viscosity. We realize that the wave propagation characteristics will be affected by the turbulence, but we also are unaware of any generally accepted method for accounting for such effects. If one considers the dynamical equation for \tilde{u} in the presence of turbulence, as presented by Reynolds & Hussain (1972; equation 2.6), new unknown terms appear, such as the time and phase average of $u'v'$. The simplest way to account for the effects of turbulence is to use an eddy viscosity along with the turbulent base flow as done by Tam & Chen (1979), Liu (1971), Potter (1971), and others. If we adopt a similar model here and replace the molecular kinematic viscosity with an eddy viscosity in (4), this approach leads to a possible explanation regarding the difference in behaviour of the sinuous and varicose modes shown in figure 13(a, b). The magnitude of the eddy viscosity was estimated from our recent Reynolds-stress measurements in the unforced wake of the flat plate. These results indicate that the eddy viscosity is, on

the average, 40 lines larger than the kinematic viscosity of the fluid, so the effective Reynolds number for the present data becomes $(Re_\theta)_{\text{eff}} = 30$. Therefore, if one wants to lump the nonlinear effects stemming from the generation of Reynolds stresses (whether coherent or random) into a model represented by an eddy viscosity, then one should use an effective Re_θ which is based on ν_T . It is apparent from figure 14(c) that, at this lower Reynolds number, the sinuous mode is still amplified, although at a smaller rate. On the other hand, figure 15(c) shows that the varicose mode is damped over the entire experimental domain in accordance with the experimental results shown in figure 13(b). The eddy-viscosity model brings improvement to the prediction of the streamwise variation, especially for the varicose mode. Figure 13(a, b) shows the spatial development of the maximum of the two modes. The dashed lines correspond to the calculation using the eddy-viscosity model with $Re_\theta = 30$. The transverse distributions of the \tilde{u} -amplitudes are also well explained, as shown in figure 16(a, b). The dotted-dashed lines represent the eddy-viscosity calculations using $Re_\theta = 30$. A comparison with the measured distributions shows that, although the general features of the amplitude distributions are predicted quite well, the computed distributions are wider than their measured counterparts. This is undoubtedly caused by the significantly higher values of viscosity used in the $Re_\theta = 30$ case. Also, although not shown here, the phase distribution for the varicose case is not well predicted (see Marasli 1988). Summarizing these results, linear stability theory predicts the local shapes of the eigenfunction distributions for both modes fairly well, while slowly diverging linear theory does a reasonable job for the streamwise variation of the sinuous mode. On the other hand, the eddy-viscosity model predicts the streamwise variation of both modes reasonably well and describes the transverse distributions of the perturbation amplitudes for both modes, but it fails to predict the distribution of phase for the varicose mode.

The difficulty encountered in generating a varicose disturbance that survived in the far wake is more understandable through this model. Recall, however, that the slowly diverging analysis predicts larger overall amplification for the varicose mode than the sinuous mode in a laminar base flow. For particular wake-generator configurations, the near wakes in a laminar flow could be dominated by varicose instabilities (see, for example, Williamson 1985; Rockwell *et al.* 1985; and Papailiou & Lykoudis 1974). This does not mean that the varicose mode is the dominant instability for the near wakes. For the varicose mode to have a chance, the Reynolds number must be high enough to avoid the viscous effects; on the other hand, the flow must also be free of incoherent fluctuations to maintain a laminar base flow.

The eddy-viscosity model appears to be adequate for understanding some of the features of travelling waves in a fully turbulent base flow; however, its shortcomings have to be kept in perspective. In addition to its problems of describing turbulent flows in general, the fact that turbulence reorganizes itself by interacting with the coherent motion (Hussain 1983; Marasli 1988) is an additional complexity which cannot be described by this model. Nevertheless, a conceptual simplification of the effects of incoherent turbulent fluctuations is provided by this model.

10. Conclusions

It is possible to generate a nearly pure varicose mode of instability in the wake. The sensitivity of the flow to asymmetric disturbances, however, makes it a difficult experimental task. Even the slightest asymmetric disturbance can be preferentially amplified, as the growth rates of sinuous disturbances are much larger than those for

varicose disturbances. Therefore, contamination of the varicose mode by the sinuous mode is difficult to avoid, especially over large downstream distances.

A decomposition technique was developed to separate a phase-averaged distribution into its symmetric and antisymmetric components. The measurements show that these components agree well with their corresponding theoretical counterparts, that is, the varicose and sinuous modes from linear stability theory. The relative strength of the two modes at any downstream location can then be determined by integrating the amplitude distribution across the flow for each mode and taking the ratio of the two. The modal decomposition technique was applied to a case of combined excitation. The relative-strength-ratio measurements show that, initially, the varicose mode was twice as strong as the sinuous mode, but the sinuous mode eventually became dominant because of the larger amplification rates. An equilibrium ratio was approached in the far wake for $x/\theta > 1000$.

Viscosity affects the varicose mode more than it does the sinuous mode. As expected, the amplification rates were found to decrease with decreasing Reynolds number and velocity deficit, but the phase speed of the disturbance remains unaffected. An attempt to account for the effects of turbulence on the spatial propagation of a perturbation wave was made using an eddy-viscosity model. Based on this model, a possible explanation was obtained for the observed discrepancy between the experimental results and the slowly diverging wake prediction for the varicose mode.

This project was supported by the Air Force Office of Scientific Research under contract no. 85-00148. We wish to thank Dr James M. McMichael for his efforts in monitoring the project. We also would like to thank Dr T. F. Balsa for his cooperation in determining the validity of some of our stability calculations.

REFERENCES

- BELLMAN, R. E. & KALABA, R. E. 1965 *Quasilinearization and Nonlinear Boundary Value Problems*. Elsevier.
- BETCHOV, R. & SZEWCZYK, A. 1963 *Phys. Fluids* **6**, 1391.
- HUSSAIN, A. K. M. F. 1983 *Phys. Fluids* **26**, 2816.
- LIU, J. T. C. 1971 *Phys. Fluids* **14**, 2251.
- MARASLI, B. 1988 Spatially traveling disturbances in a plane, turbulent wake. Ph.D. thesis, University of Arizona.
- PAPAILIOU, D. D. & LYKOUDIS, P. S. 1974 *J. Fluid Mech.* **62**, 11.
- POTTER, M. C. 1971 *Phys. Fluids* **14**, 1323.
- REYNOLDS, W. C. & HUSSAIN, A. K. M. F. 1972 *J. Fluid Mech.* **54**, 263.
- ROCKWELL, D., ONGOREN, A. & UNAL, M. 1985 AIAA paper 85-0529, presented at *AIAA Shear Flow Control Conference*, Boulder.
- TAM, C. K. W. & CHEN, K. C. 1979 *J. Fluid Mech.* **92**, 303.
- WAZZAN, A. R., OKAMURA, T. T. & SMITH, A. M. O. 1968 Spatial and temporal stability charts for the Falkner-Skan boundary-layer profiles. Rep. DAC-67086. Douglas Aircraft Company, Long Beach.
- WILLIAMSON, C. H. K. 1985 *J. Fluid Mech.* **159**, 1.
- WYGNANSKI, L., CHAMPAGNE, F. H. & MARASLI, B. 1986 *J. Fluid Mech.* **168**, 31.